

pubs.acs.org/acssensors Article

Inkjet-Printed Wearable E-nose with Liquid-Phase Ligand-Exchanged Quantum Dots for Human-Centered Gas/Odor Monitoring

Zhu'an Wan, Weiqi Zhang, Suman Ma, Zhilong Song, Chen Wang, Yucheng Ding, Chak Lam Jonathan Chan, Feng Xue, Zixi Wan, Wenhao Ye, and Zhiyong Fan*



Cite This: https://doi.org/10.1021/acssensors.5c01908



ACCESS I

III Metrics & More

Article Recommendations

Supporting Information

ABSTRACT: The development of next-generation wearable electronic nose (e-nose) systems for real-time environmental monitoring requires miniaturized gas sensor arrays with high sensitivity and low-power operation. Current limitations persist in the incompatibility between conventional sensing material deposition methods and MEMS microheater architectures. Here, we present an intelligent wristwatch-formatted e-nose system, integrating a printable quantum dot (QD) sensor array fabricated using an optimized colloidal quantum dot (CQD) ink formulation and a precision inkjet printing strategy. We engineered metal cation-surrounded quantum dots (MCSQDs) via liquid-phase ligand exchange with transition metal chlorides (FeCl₃, CoCl₂,



NiCl₂, CuCl₂), achieving tailored surface functionalities and enhanced gas discrimination capabilities. The engineered MCSQD inks demonstrated exceptional colloidal stability and seamless MEMS microheater integration, enabling gas sensors with parts-per-billion-level detection limits (4 ppb ethanol). A 16-unit sensor array was embedded into a wearable platform incorporating cloud-based neural network processing. System validation achieved 100% classification accuracy in indoor odor recognition tests using a fully connected neural network (FCNN), while field tests at a transportation hub demonstrated reliable monitoring of Total Volatile Organic Compounds (TVOC), NO₂, SO₂, and CO with <15% deviation from the reference sensors. This work establishes a viable manufacturing framework bridging quantum-confined material engineering to IoT-enabled artificial olfaction, paving the way for scalable production of QD gas sensor array-based e-noses.

KEYWORDS: wearable electronic nose, colloidal quantum dot, inkjet printing, human-centered gas monitoring, liquid-phase ligand exchange

lectronic noses (e-nose), termed artificial olfactory systems, are bioinspired sensing devices that imitate the function of the mammalian olfaction^{1,2} through cross-sensitive gas sensor arrays coupled with machine learning algorithms. These systems perform odor discrimination and chemical analysis by translating gas-receptor interactions into multivariate signal patterns, demonstrating exceptional versatility in the detection of complex volatile organic compounds (VOCs), hazardous pollutants, and biochemical markers. The convergence with emerging paradigms, such as the Internet of Things (IoT) and wearable electronics, has established a critical technological imperative for the development of miniaturized e-nose platforms that merge small size, high sensitivity, and good discrimination capability. Modern wearable e-nose³ enables human-centric applications, such as real-time detection of flammable/toxic species in the environment and breath analysis via exhaled VOC profiling for personal healthcare. However, the development of wearable enoses faces significant challenges, particularly the need for

miniaturized and highly informative gas sensor arrays that constitute the core components of these systems.

Among the prevailing gas-sensing technologies, MEMS-integrated metal oxide semiconductor (MOS) gas sensors exhibit unparalleled advantages for constructing miniaturized sensor arrays, outperforming their electrochemical and optical counterparts in scalability and CMOS compatibility. In recent years, numerous innovative studies have focused on enoses based on MEMS-integrated MOS gas sensor arrays. To incorporate different sensing materials and achieve diverse sensing properties in gas sensor arrays, individual material

Received: June 1, 2025 Revised: October 10, 2025 Accepted: October 24, 2025



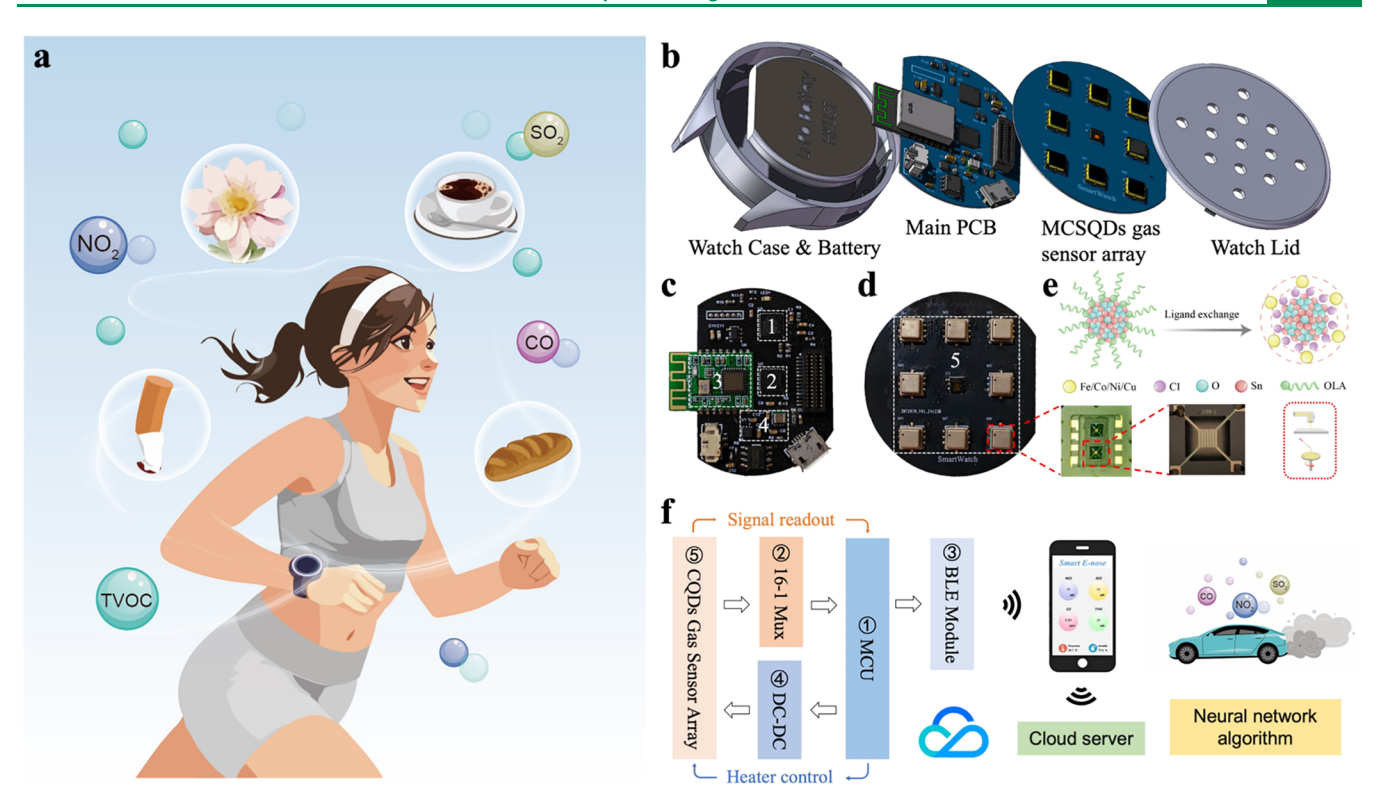


Figure 1. Schematic diagram of a wearable e-nose system with a printable quantum dot gas sensor array for human-centered gas monitoring. (a) Diagram of wristwatch-style smart e-nose worn by a running woman; (b) schematic diagram of the e-nose system, including watch case, lithium battery, main PCB, MCSDQ gas sensor array, and watch lid; (c) photographs of main PCB; (d) photographs of the MCSDQ gas sensor array board; (e) illustration of the ligand exchange process and device fabrication process; and (f) system diagram of e-nose working with mobile phone and cloud server.

deposition on each sensing unit is required. Standard semiconductor deposition techniques (e.g., magnetron sputtering deposition, atomic layer deposition) demonstrate superior compatibility with MEMS-based microheater substrates and are widely adopted for MEMS gas sensor array fabrication. 13-16 However, sensitive materials deposited by these processes form relatively compact films, which generally show limited sensitivity, struggling to detect gases at ppb levels. Some derivative PVD techniques, such as glancing angle deposition¹⁷ (GLAD) and oblique angle deposition¹¹ (OAD), can also be used to fabricate high-surface-area gas-sensitive materials on MEMS platforms, thereby achieving enhanced sensitivity. Nevertheless, these advanced techniques involve complex processes and require substantially more processing time when sequentially depositing different sensing materials. Besides, dispensing and traditional printing methods enable the deposition of diverse high-performance gas-sensitive materials during traditional ceramic microhot plate device fabrication. However, they exhibit critical incompatibilities with MEMS microheaters, manifested as insufficient deposition positioning accuracy, film uniformity, and poor interfacial adhesion. In contrast, the inkjet printing 8-10,18,19 method has emerged as an effective and efficient manufacturing approach for functional electronics. It takes advantage of maskless patterning with a sub-100 μ m resolution and material conservation through drop-on-demand ejection. Especially for MEMS-integrated gas sensor array development, 20 this method provides a streamlined process from material preparation to device fabrication, allowing for smooth integration and enhanced design flexibility with different printable inks.

Typical gas-sensing materials, such as SnO₂- and ZnO-based materials, 21,22 grown by the hydrothermal method, have been integrated into gas sensors using the inkjet printing method and have demonstrated good performance. Among emerging printable materials, colloidal quantum dots (CQDs)^{23,24} have attracted wide attention due to their superior gas-sensing performance and intrinsic solution processability. The nanoscale grain size^{25,26} of CQD leads to an ultrahigh surface-tovolume ratio, facilitating enhanced gas adsorption and sensitivity. Furthermore, the tunable surface chemistry, enabled by ligand engineering, 27,28 allows selective functionalization for diverse sensing properties, which is critical for the crossreactive gas sensor array development. Despite these advantages, CQD-based gas sensors remain predominantly confined to single-pixel devices, with limited progress toward scalable array fabrication. Key challenges arise from the complexity of ligand removal and making diverse sensing materials.

To address these limitations, we propose herein an approach involving metal cation-surrounded SnO_2 quantum dots synthesized via liquid-phase ligand exchange, combined with inkjet printing to fabricate gas sensor arrays. The hydrothermal method²⁹ is used to synthesize SnO_2 quantum dots stabilized by oleic acid and oleylamine ligands. A liquid-phase ligand exchange treatment^{30–32} is applied to the as-synthesized quantum dots with four types of transition metal chloride solutions. The long-chain organic ligands of quantum dots are replaced by small chloride ions balanced with metal cations, forming metal cation-surrounded quantum dots (MCSQDs) with good colloidal stability. Optimized MCSQD inks are inkjet-printed on commercial MEMS microheaters, achieving a

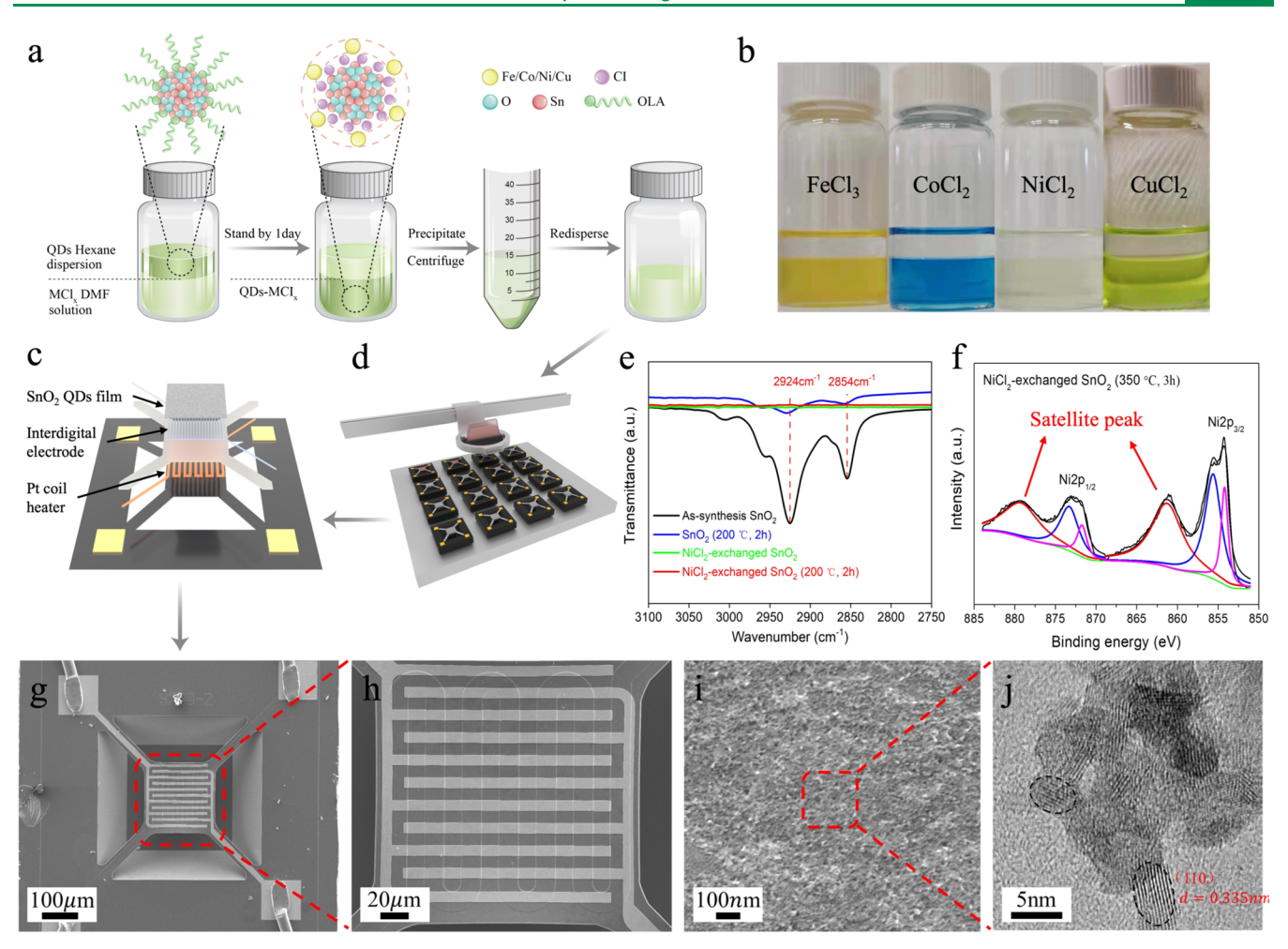


Figure 2. Illustration of ligand exchange process, device fabrication process, and characterizations. (a) Schematic of the ligand exchange process to prepare MCSQD ink with 4 kinds of metal chlorides; (b) photographs of ligand exchange; (c) schematic diagram of the MEMS device; (d) schematic diagram of MCSQD ink printing on the MEMS device. (e–j) Characterizations of NiCl₂ exchanged MCSQD film: (e) FTIR spectrum; (f) XPS spectrum; (g–i) SEM images of the printed MCSQD film on the device; and (j) TEM image of annealed MCSQDs.

robust and crack-free thin film. The resulting SnO_2 QD gas sensors exhibit digit ppb limits of detection (4 ppb ethanol) and good stability. Moreover, gas sensors fabricated using MCSQD inks exhibit distinct sensing characteristics depending on the specific metal chloride used, enabling the constructed sensor array to demonstrate exceptional gas discrimination performance.

Furthermore, a wrist-worn e-nose system with a 16-pixel gas sensor array, shown in Figure 1b, is designed for dual-mode human-centered gas detection: indoor odor classification and outdoor environmental monitoring. In controlled indoor trials, the system achieved 100% discrimination accuracy for five common odors (alcohol, cigarette smoke, pet excrement, food, and furniture) using a fully connected neural network (FCNN). Field deployment at a semi-open transportation hub demonstrated concurrent monitoring of four hazardous environmental gases, namely total volatile organic compounds (TVOC), nitrogen dioxide (NO₂), sulfur dioxide (SO₂), and carbon monoxide (CO). The errors of the predicted concentrations of four gases by the e-nose system compared with those of the reference photoionization sensor and electrochemical sensors are 13.3% (TVOC), 8.3% (NO₂), 5.7% (SO₂), and 15.3% (CO), respectively.

This work pioneers the liquid-phase ligand exchange method to synthesize diverse MCSQDs inks, enabling direct MEMS-compatible inkjet printing of ultrasensitive arrays and bridging the gap between nanomaterial innovation and practical artificial olfaction for environmental health monitoring.

■ RESULTS AND DISCUSSION

Wearable E-nose System Design. A wristwatch-style wearable electronic nose system has been developed by employing MCSQD gas sensor arrays as the core sensing elements. As illustrated in Figure 1b, the system comprises four primary components: a watch enclosure, a power supply unit, a main control board, and a gas sensor array. The main board (Figure 1c) performs three critical functions: (1) supplying regulated heating voltages to the sensor array, (2) acquiring and processing analog signals from the gas sensor array, and (3) transmitting digitized data via low-power Bluetooth to paired mobile devices. The gas sensor array configuration (Figure 1d) features 8 lead ceramic packages (5 mm × 5 mm each), with dual heterogeneous sensors integrated per package, yielding a total of 16 distinct sensing elements inkjet-printed from different MCSQD inks. The corresponding schematics are shown in Figure S1.

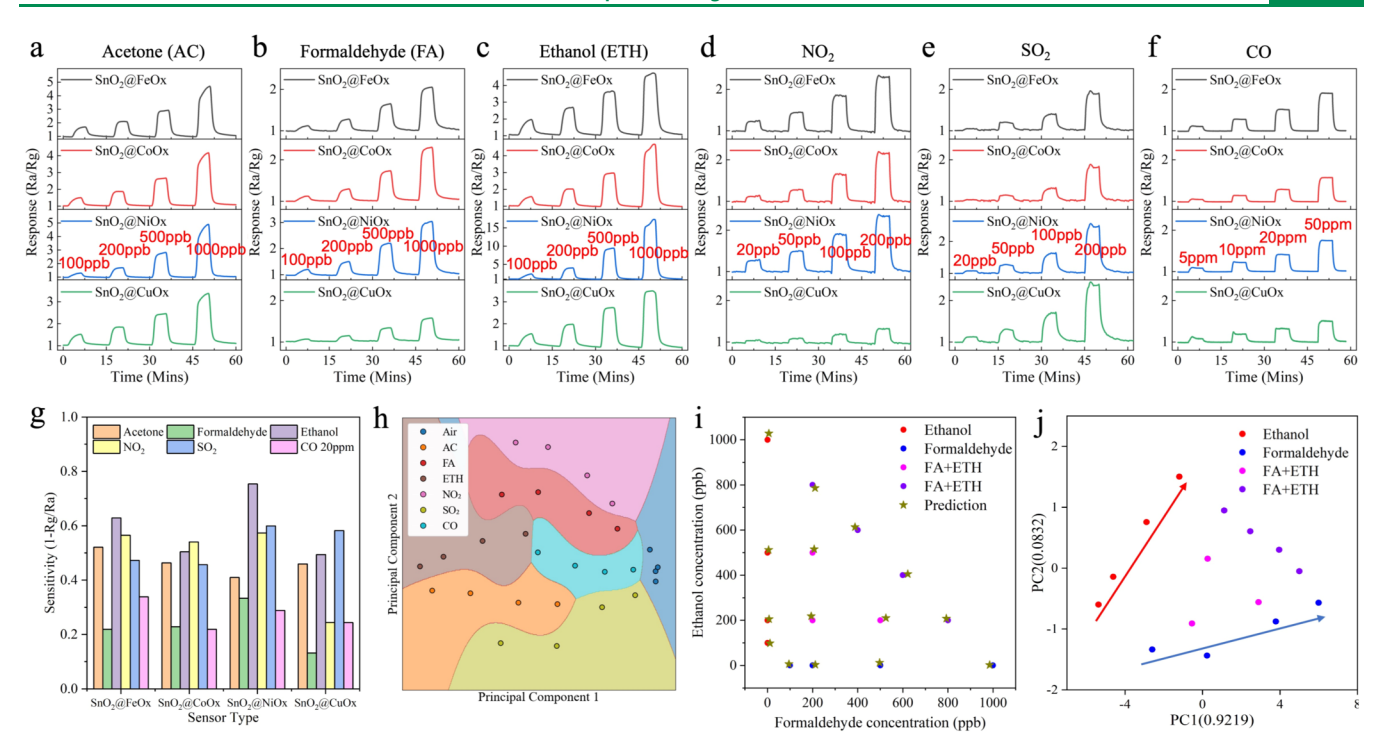


Figure 3. Gas-sensing properties of 4 types of MCSQD gas sensors with working temperature of 300 °C. (a–f) Sensing curves of gases under 60% relative humidity: 100/200/500/1000 ppb (a) acetone, (b) formaldehyde, (c) ethanol; 20/50/100/200 ppb (d) NO₂, and (e) SO₂; 5/10/20/50 ppm (f) CO. (g) Selectivity of the MCSQD gas sensors; (h) gas classification results with PCA and SVC algorithm. (i) Prediction results of the formaldehyde and ethanol mixture gas test; and (j) PCA results of the mixture gas test.

Signal acquisition employs a 16-to-1 analog multiplexer that sequentially routes the sensor outputs to a unity-gain buffer stage before analog-to-digital conversion via the microcontroller unit (MCU)'s integrated 12-bit ADC. Real-time sensor resistances are calculated using Ohm's law from the measured voltage values, quantitatively reflecting the gas response.³³ A commercial temperature and humidity sensor is also integrated. The complete system workflow, depicted in Figure 1f, demonstrates the cloud-based neural network processing of raw data with final visualization on the mobile app.

Power management represents a critical design consideration for wearable devices. The system integrates an 800 mAh rechargeable lithium-ion battery, supporting continuous operation exceeding 7 h. With the sensor array consuming around 400 mW (25 mW/sensor) as the dominant power load, system-wide consumption remains at approximately 450 mW, accounting for the auxiliary components (MCU, op-amps, and Bluetooth). Implementing intermittent operation strategies³⁴ (10% sensor duty cycle) could theoretically extend the operational duration to approximately 72 h. However, gassensing tests demonstrate that intermittent operation compromises sensor performance, resulting in reduced sensitivity (Figure S16), slower response/recovery dynamics, and potentially diminished humidity interference resistance and long-term stability. Therefore, achieving significant power reduction in e-nose systems requires more effort in device architecture optimization and energy-harvesting methods in future work.

Characterization of MCSQDs. The metal cations surrounding the SnO₂ quantum dots were synthesized via liquid-phase ligand exchange between presynthesized SnO₂ quantum dots in hexane and dimethylformamide (DMF)

solutions containing transition metal chlorides (FeCl₂, CoCl₂, NiCl₂, or CuCl₂). The procedures for ligand exchange and ink formulation are illustrated in Figure 1a, with the details provided in the methods and mechanisms discussion presented in Supplementary Notes 1 and 2. The resultant MCSQDs formed a stable colloidal dispersion in methanol, exhibiting pronounced Tyndall scattering (Figure S2). Optical bandgap analysis was performed through UV-vis absorption measurements on both pristine SnO2 quantum dots in hexane and the NiCl₂-treated MCSQD ink. Tauc plots derived from these measurements (Figure S3) revealed a bandgap energy of 4.05 eV for both systems, significantly larger than bulk SnO₂ (3.5 eV), confirming quantum confinement effects after ligand exchange. Remarkably, the MCSQD dispersions maintained colloidal stability via electrostatic stabilization for over three years. This stabilization mechanism was confirmed by zeta potential measurements at +35 mV (Figure S6a), well above the typical stability threshold (>30 mV), indicating strong electrostatic repulsion. Although visual inspection (Figure S5) showed no significant precipitation or turbidity, dynamic light scattering (DLS) measurements (Figure S6b) indicated minor agglomeration over time.

To systematically investigate the effect of metal cation modulation on the sensing properties, four distinct concentrations of each transition metal salt were reacted with pristine SnO_2 quantum dots, yielding 16 compositionally tailored inks. Remarkably, ink printability was achieved solely through the addition of ethylene glycol, with no surfactants or other additives due to their intrinsic colloidal stability.

MCSQD inks were deposited on a plasma-treated microheater substrate integrated with interdigitated sensing electrodes, as schematically illustrated in Figure 2c. Scanning electron microscopy (SEM) images (Figure 2g—i) revealed densely

packed nanoparticles in the deposited films. High-resolution transmission electron microscopy (HRTEM) images (Figures 2j and S4) conclusively demonstrated that the quantum dots maintained their morphology ($\sim\!\!5$ nm diameter) across all processing stages, from synthesis and ligand exchange to the film on the device after printing and annealing. These results confirm that the ligand exchange procedures maintain the ultrasmall dimensions of the SnO_2 quantum dots without structural degradation.

Surface chemistry analysis was performed to further reveal the ligand exchange process and the surface modification of the resulting quantum dot sensing film. Fourier-transform infrared (FTIR) spectroscopy of pristine SnO₂ (Figure 2e, black curve) exhibited characteristic C-H stretching vibrations (2924 and 2854 cm⁻¹) from residual hydrocarbon ligands, persisting even after mild annealing. In contrast, the NiCl2-treated samples (green and red curves) showed complete elimination of these peaks, confirming efficient ligand removal via liquid-phase ligand exchange. The samples treated with other metal chlorides consistently yielded the same results (Figure S8). Following liquid-phase ligand exchange, transition metal cations (e.g., Fe³⁺, Co²⁺, Ni²⁺, and Cu²⁺) are bound to the SnO₂ QD surface as chlorides. Subsequent high-temperature annealing (350 °C, 3 h) transformed these metal chlorides into their respective metal oxide species, as evidenced by X-ray photoelectron spectroscopy (XPS) analysis of the annealed films. The Ni 2p spectrum (Figure 2f) displayed distinct satellite features indicative of NiO formation, validating the oxidation of the transition metal ions during thermal processing. Analogous behavior was observed in the CoCl₂ and CuCl₂ treatments (Figure S9). Further supporting the conversion, XPS (Figure S10b) and TEM-EDS analyses (Figure S12) both revealed a significant reduction in the chlorine (Cl) content compared with the original chlorides. XPS analysis also indicated that the atomic ratios of the modifying metal elements (e.g., Ni, Co, and Cu) to Sn were mostly below 0.15 (Figure S10a). Furthermore, the XRD characterization of the annealed materials showed no distinct diffraction peaks, which could be attributed to the modified metal oxides (Figure S11). This combined evidence suggests that the modified metal oxide species exist on the SnO₂ QD surfaces in a relatively dispersed state. This dispersed metal oxide modification on the SnO2 QD surface creates local heterojunctions,³⁵ which significantly enhance and modulate the gas-sensing properties.

Gas-Sensing Performance of the MCSQD Sensor Array. The gas-sensing evaluation of the MCSQD sensors systematically tested three TVOC targets (acetone, formaldehyde, ethanol) and three environmental pollutants (NO₂, SO₂, and CO) under application-relevant concentration gradients using the measurement system mentioned in the Methods. Figure 3a-f present the real-time response-recovery curves of the four representative sensors. From top to bottom in each panel, the sensors correspond to the FeO_x -, CoO_x -, NiO_x-, and CuO_x-surface-modified SnO₂ quantum dot devices. The developed MCSQD gas sensors demonstrate excellent repeatability in terms of the response-recovery characteristics and baseline stability. To further assess repeatability, cyclic response-recovery tests with 100 ppb ethanol gas were performed over 100 cycles, with fluctuations in both the response and baseline remaining below 1% (Figure S13).

Notably, particular sensors exhibited exceptional individual performance. The NiO-modified sensor achieved remarkable

detection limits of 4 ppb for ethanol and 15 ppb for acetone (evaluated in Figure S14). Based on our limited literature review, the developed sensors demonstrate superior sensitivity to ethanol and acetone compared to other reported sensors while exhibiting moderate sensitivity to NO₂, SO₂, and CO. The performance comparisons with other reported sensors are summarized in Table S1. Long-term stability evaluation revealed a small performance degradation during the 6 weeks of continuous testing (Figure S15). Evaluation of the sensor performance under different humidity conditions (Figures S16 and S17) revealed that high humidity slightly reduced the gas sensitivity.

All sensors exhibited p-type responses to NO₂, with resistance decreasing across the tested concentrations, attributed to localized heterojunctions formed by transition metal oxide modification on SnO₂ quantum dot surfaces. Furthermore, these local p-n junctions or heterojunctions simultaneously enhance gas sensing through electrical and chemical catalytic pathways. Electrically, the induced heterojunctions create a deeper electron depletion layer, significantly raising the material's baseline resistance. When reducing gases react, the released electrons neutralize the additional space charge within this layer, lowering the potential barrier and causing a substantial resistance drop that boosts sensitivity. Catalytically, the modified metal oxides facilitate sensing by lowering the activation energies for specific gas reactions, promoting adsorption, and surface reactivity due to their distinct affinities and catalytic activities. The impact of modifying metal oxides on gas-sensing performance varies depending on their type and concentration. This variation enabled the construction of the sensor array in this work, which utilizes SnO2 QDs modified with varying types and concentrations of metal oxides.

Although individual sensors exhibited unique merits, the array's collective capability for complex odor discrimination constitutes the core advancement of this work. Figure 3g displays the responses (calculated as $1 - R_g/R_a$) of the four sensors to different gases at identical concentrations, revealing discernible selectivity variations among them. The response magnitude versus concentration profiles for each sensor are also presented in Figure S18, providing a more comprehensive view of the differences in selectivity. Principal component analysis (PCA) was employed for dimensionality reduction and visualization of response features. Figure 3h shows the clear separation of different gas concentrations in the 2D PCA space. The decision boundaries defined by the support vector classification (SVC) further validated the sensor array's capability to effectively distinguish between different gas species. In addition, experiments reveal that humidity impairs gas discrimination in electronic noses (Figure S19), though incorporating humidity sensor data for algorithmic compensation can mitigate this effect.

To simulate a typical indoor environment, gas mixtures of formaldehyde and ethanol were tested at specific concentration combinations, as shown in Figure 3i. One test round provided training data, and a separate round served as validation data. Only one set of stable response data was taken as the representative feature for each gas concentration combination. Using a fully connected neural network (FCNN) algorithm, the concentrations of both compounds were quantified with a relative error of <5%. The predicted results are also plotted along with the corresponding test concentration combinations in Figure 3i. Furthermore, PCA analysis of the training data is

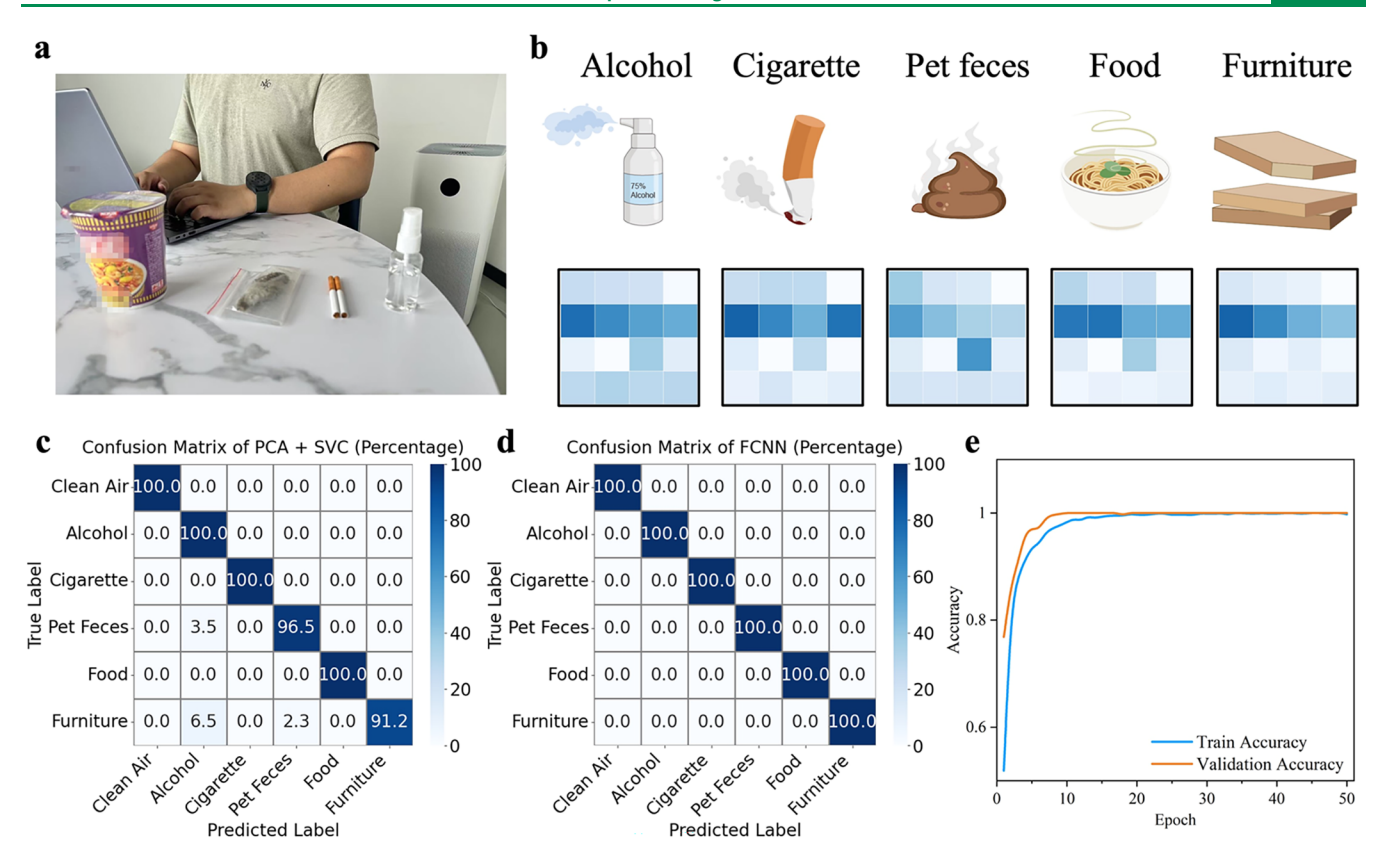


Figure 4. Indoor odor classification. (a) Photo of the experimental situation; (b) normalized response patterns for common indoor odors, including alcohol spray, cigarette smoke, pet feces, food, and furniture; (c) confusion matrix of odor classification with the PCA + SVC algorithm; (d) confusion matrix of odor classification with the FCNN algorithm; and (e) accuracy curves during training and validation versus epoch.

presented in Figure 3j. Different colored dots represent the measured data features of the ethanol single-component, formaldehyde single-component, and ethanol—formaldehyde gas mixtures, respectively. Their distribution patterns align with the gas concentration combinations shown in Figure 3i, thus demonstrating that the data features effectively capture the concentration information for both gases.

These comprehensive evaluations substantiate the outstanding gas-sensing performance and practical potential of the developed MCSQD gas sensor array. The diversity of sensing elements, combined with a robust pattern recognition algorithm, positions this MCSQD gas sensor array as a promising platform for complex odor monitoring applications.

Indoor Odor Classification. The wearable e-nose system was employed for indoor odor monitoring and classification, which holds significant implications for maintaining healthy indoor environments.³⁶ Traditional air quality modules in air purifiers rely on passive odor detection after gas diffusion to the device, resulting in diluted contaminant readings and delayed responses. Their single-sensor designs, lacking interference resistance, are prone to false activation, resulting in unnecessary energy consumption and noise. Conversely, a wearable e-nose system overcomes these constraints through human-centered odor tracking and odor classification capability to enhance the detection accuracy and activation timeliness. As depicted in Figure 4a, the experiments were conducted in a controlled room simulating typical indoor conditions. Testing was conducted by bringing the wrist-worn e-nose system close to the odor source. However, some odor samples were released in a short time or a certain amount by the control and diffused throughout the room until equilibrium was reached. After testing, the two fans connected to the outdoors were activated: one drew fresh air into the testing room, while the other exhausted residual gases from the room to the outdoors, accelerating the replacement of residual odors in the room with relatively clean air.

Figure 4b presents the normalized response patterns of the 16-unit sensor array for five indoor odor categories: alcohol, cigarette smoke, pet feces, food, and furniture emissions. Here, food is represented by instant noodles of various flavors, while furniture is symbolized by low-quality composite laminates. Distinct response profiles across odor sources established the foundation for subsequent classification analyses.

To enhance dataset diversity, multiple odor source samples with subtle differences or release amounts for each category were tested. Data labeling was performed using a standardized protocol: only response segments between 80% peak/steady-state signal attainment (based on Sensor 1's response) and purge initiation were retained, as visualized in Figure S20. For slow-emitting odors (e.g., pet feces and furniture), labeling commenced at a lower response threshold. Approximately 1000 data groups per category (including clean air) were collected, with 50% randomly assigned to the training sets and the remainder for validation.

Classification results using principal component analysis with a support vector classifier (PCA-SVC) achieved a 95.3% overall accuracy (Figure 4c). Category-specific accuracies were 91.2% (furniture), 100% (food), 96.5% (pet feces), 100% (cigarettes), and 100% (alcohol). Notably, a fully connected neural network algorithm (FCNN) achieved 100% classification accuracy, demonstrating the superior odor discrimination capability of the e-nose system. The training progression, as

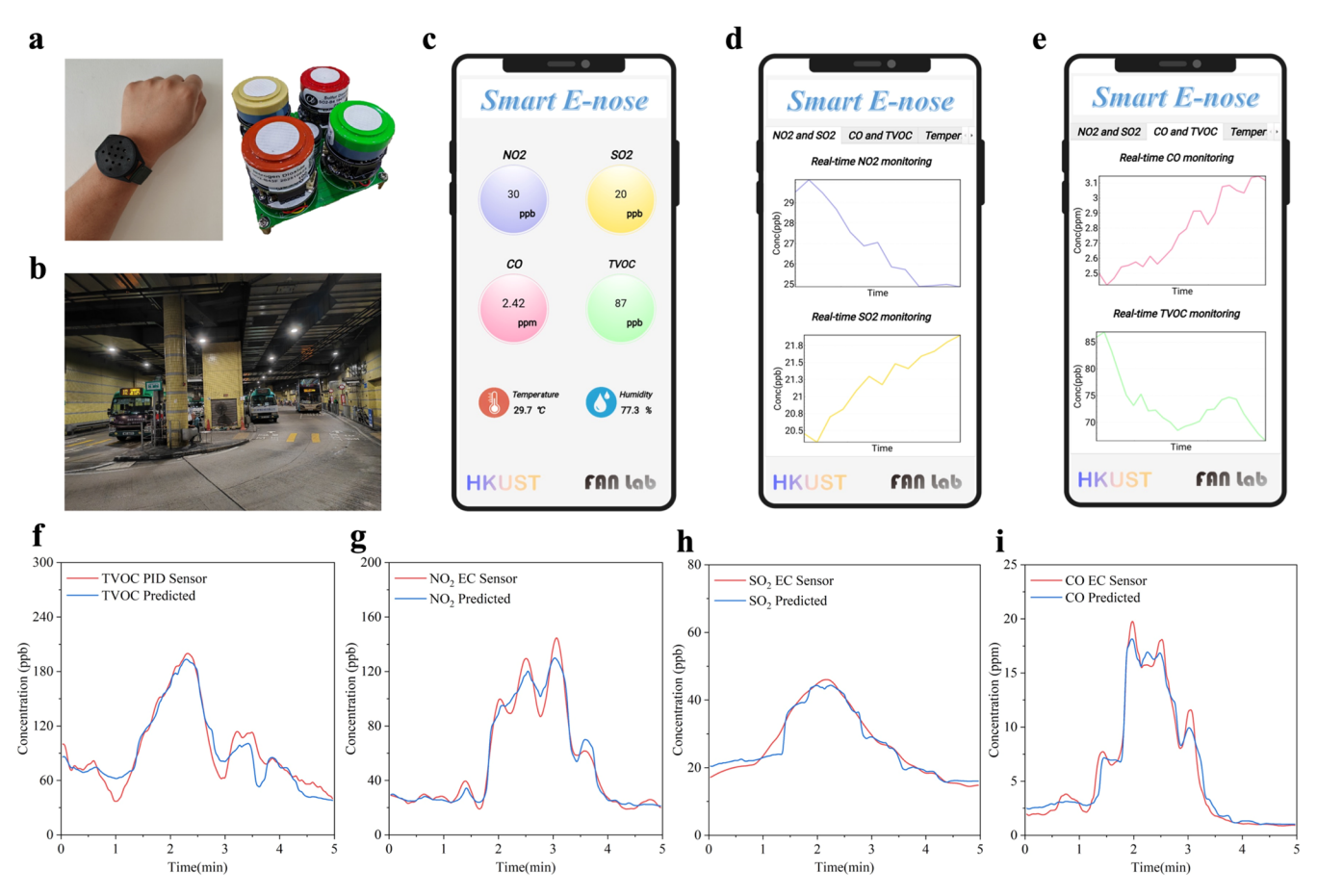


Figure 5. Outdoor hazardous gas monitoring. (a) Photo of wearable e-nose, photoionization detector (PID), and electrochemical (EC) gas sensors as reference for e-nose training, PID sensor for TVOC and EC sensors for NO_2 , SO_2 and CO. (b) Photo of the experimental situation in a transportation hub; (c–e) gas concentrations and their curves predicted by the e-nose system shown in the mobile app; (f, g) comparison of concentration curves between the e-nose system and reference gas sensors: (f) TVOC, (g) NO_2 , (h) SO_2 , and (i) CO.

shown in Figure 4e, revealed rapid convergence of both the training and validation accuracy curves, indicating a stable algorithmic parameter optimization. Furthermore, the e-nose system was capable of analyzing fruit ripeness, with the corresponding data illustrated in Figure S21.

Outdoor Hazardous Gases Monitoring. Another demonstration involved implementing a wearable e-nose to monitor pollutant gases in commuters' ambient environments, offering significant benefits for public health and environmental management. In this experiment, commercial photoionization sensors and electrochemical sensors served as reference devices for e-nose system training and validation (Figure 5a), pre-calibrated for four target gases: isobutylene, NO₂, SO₂, and CO. The testing environment was a semienclosed transportation hub (Figure 5b). A mobile application was developed to receive Bluetooth-transmitted data from an e-nose. Raw data from the mobile device were uploaded to a cloud server, where the analytical algorithms predicted gas concentrations before visualization in the app. The real-time gas concentration, temperature, and humidity readings are presented in Figure 5c-e, accompanied by their temporal variation curves.

A 5-layer fully connected neural network (architecture: 18-128-64-64-32-4 nodes) was employed for algorithm development. Input features comprised response data from 16 gas sensors plus temperature/humidity readings (18 parameters in total), while concentrations from four reference sensors served

as prediction targets. The training data consisted of two sequential shuttle tests conducted at the transportation hub, with the detailed training outcomes shown in Figure S22. Following the algorithm training and deployment, the system's performance was validated using data from a third shuttle test, as recorded in Video S1. Comparative results between the enose predictions and reference sensor measurements for various gases during testing (Figure 5f-i) revealed closely aligned temporal trends with relative errors of approximately 15%. Although the e-nose demonstrated reasonable performance, we attribute this partly to the relatively simplified test environment with minor humidity fluctuations, stable gas compositions, and consistent concentration trends. This is reflected by the e-nose response data and PCA analysis (Figures S23 and S24). Figure S25 presents a progressively decreasing mean absolute error (MAE) with training epochs, obtained by retraining the network with new test data as a validation dataset. Error reduction on the validation data outpaced that on the training data, demonstrating that the gas sensor array can effectively reflect the concentration changes of multiple gases.

A comparative table (Table S2) is presented to benchmark our e-nose against the reported e-nose systems, particularly the MEMS-based sensor arrays. Given the favorable sensitivity and stability of this e-nose, there is significant potential for its practical use in specific scenarios as wearable gas monitoring devices, through future efforts involving the establishment of

more comprehensive dataset and further algorithm optimization. Expanding the application to more wearers and diverse commuting scenarios would enable cloud-based aggregation of spatiotemporal pollution distribution data, facilitating urban digitization and environmental governance through comprehensive pollution mapping.

CONCLUSIONS

This study demonstrates a wearable e-nose system that leverages a printable colloidal quantum dot (CQD) gas sensor array for human-centered environmental monitoring. By innovating a liquid-phase ligand exchange method using transition metal chlorides, we synthesized stable MCSQD inks that overcome traditional CQD processing limitations, enabling the scalable fabrication of highly sensitive MEMS sensor arrays. The resultant 16-sensor array exhibited ppb-level detection limits and diverse gas-sensing characteristics, attributed to the large surface area and high-surface reactivity of quantum dots combined with the enhancing effects of transition metal oxide modifiers. Integrated into a wristwatch platform with neural network-driven cloud analytics, the system achieved 100% accuracy in indoor odor classification and reliable outdoor pollution monitoring with <17% error against reference sensors. The integration of printable MCSQD ink synthesis, MEMS gas sensor technology, and AI-driven data processing has created a breakthrough platform for wearable artificial olfactory systems. Future work will focus on expanding the library of printable QD inks, optimizing the power efficiency, and developing scenario-adaptive algorithms to enable comprehensive human-centered gas monitoring across daily life and occupational scenarios. This technology has significant potential for personalized healthcare, IoT-driven air quality management, and smart cities.

METHODS

SnO₂ Quantum Dot Synthesis. 0.6 g of SnCl₄·5H₂O is added to 20 mL of oleic acid precursor solvent as a Sn resource. Then, 2.5 mL of oleylamine is added to slightly increase the solution pH, which would also be the main surface ligand of the synthesized SnO2 QDs, along with oleic acid bonding. The mixed precursor solution is magnetically stirred vigorously for 1 h to promote the SnCl₄·5H₂O dissolution. After that, the well-dissolved precursor and 10 mL of ethanol are poured into a Teflon-lined stainless-steel autoclave for 2.5 h hydrothermal growth at 180 °C. The autoclave is cooled quickly in cold water to stop the reaction immediately after being taken out of the muffle furnace. The as-synthesized product is precipitated by adding excess ethanol, followed by centrifugation at 10,000 rpm for 6 min. The resulting precipitate is further washed twice with ethanol and then centrifuged. The final product is dispersed in 40 mL of nhexane to form a stable colloidal SnO₂ quantum dot dispersion with a concentration of 8 mg/mL (0.05 mM).

Liquid-Phase Ligand Exchange. The 0.05 mM FeCl₃, CoCl₂, NiCl₂, and CuCl₂ solutions are prepared by dissolving the corresponding masses of solid metal chlorides in *N*,*N*-dimethylformamide (DMF). Then, an equal volume of the metal chloride solution and the as-synthesized SnO₂ colloidal dispersion is mixed in a container. After standing for 1 day or undergoing ultrasound treatment, the upper hexane layer becomes clear and transparent (shown in Figure 2b), which indicates that SnO₂ quantum dots have transferred from the nonpolar hexane phase to the polar DMF phase with long-chain hydrocarbon ligands exchanged. Then, the upper hexane layer is discarded while the DMF solution at the bottom is mixed with excess toluene as an antisolvent, followed by centrifugation to precipitate the SnO₂ quantum dots. The precipitate is dispersed in 2 mL of methanol to obtain the SnO₂ MCSQD ink. The photographs taken during the process are shown in Figure S5.

Device Fabrication. The device is fabricated based on a commercial MEMS microheater (shown in Figure 2c), which can reach around 300 °C at 25 mW. First, an oxygen plasma treatment is applied to the top surface of the aforementioned microheater to make it hydrophilic. A piezoelectric inkjet printing material deposition system (DMP-2800 from FUJIFILM) is used to print the MCSQD ink on a plasma-treated substrate with interdigitated electrodes. The material cartridge with a 10 pL/drop nozzle is driven by a pattern program to print the material into a 200 μ m \times 200 μ m area 6 times. The diameter and spacing of each drop are around 50 μ m and 25 μ m, respectively. After the film deposition, the devices are annealed at 350 °C for 3 h and fixed into the chip carrier by UV epoxy and wire bonding.

The devices were also fabricated via the spin-coating process. The film morphology (Figure S26), compared with the inkjet-printing process, demonstrated a thicker structure with denser and more uniform quantum dot packing, leading to a lower sensitivity with the test results presented in Figure S27. Additionally, the reproducibility of sensors fabricated by our process is also evaluated. 32 sensors were fabricated and tested, two of which failed before the testing stage. The remaining 30 sensors exhibited relative standard deviations of 22.3% for the baseline and 20.8% for the response magnitudes (Figure S28).

Gas-Sensing Measurement. The fabricated gas sensor arrays, as mentioned above, are placed in a chamber with an inlet connected to the dynamic gas mixture system. In this system, synthetic dry air is used as both the carrying gas and balance gas to dilute the target gas from the calibrated gas cylinder. Mass flow controllers (MFCs) are applied to control the flow of target gases and balance the gas to obtain the required concentration. Signal measurement is performed by a source measure unit (SMU), namely, Keithley 2450, synchronized with a self-developed 16-channel multiplexer. The adjustable DC voltage source supplied 1.5 V to all the sensor heaters, achieving a working temperature of 300 °C with 25 mW per heater.

Characterization Method. Extensive characterization studies conducted in this work utilized the following analytical instruments: the bandgap of SnO₂ in the MCSQD ink was determined by UV—vis spectroscopy (Lambda 1050+, PerkinElmer). The composition of the surface ligands was investigated using Fourier-transform infrared spectroscopy (FTIR, Vertex 70 Hyperion 1000, Bruker) and X-ray photoelectron spectroscopy (XPS, Axis Ultra DLD, Kratos Analytical). The morphology of the printed quantum dot thin films was characterized by scanning electron microscopy (SEM, JSM-7100F, JEOL) and high-resolution transmission electron microscopy (HRTEM, JEM 2010F, JEOL).

ASSOCIATED CONTENT

Supporting Information

The Supporting Information is available free of charge at https://pubs.acs.org/doi/10.1021/acssensors.5c01908.

Schematics of the e-nose system; ligand exchange mechanism discussion; colloidal stability and mechanism discussion; photos of Tyndall effect validation; Tauc plot bandgap analysis; HRTEM of SnO₂ QDs; photos of the phase transfer ligand exchange process and QD inks; FTIR and XPS analyses of SnO₂ QD films; TEM-EDS elemental mapping; gas sensing and LOD evaluation; 6-week stability test; humidity impact on the sensing performance; raw data of the indoor odor recognition test; PCA analysis of the fruit ripeness test; raw data of the outdoor pollutant test; SEM and sensing performance comparison of inkjet printing and spin-coating film; and reproducibility evaluation. (PDF)

Video S1: human-centered hazardous gas monitoring in a transportation hub with a wearable e-nose. (MP4)

AUTHOR INFORMATION

Corresponding Author

Zhiyong Fan — Department of Electronic and Computer Engineering, The Hong Kong University of Science and Technology, Kowloon, Hong Kong SAR 999077, China; State Key Laboratory of Advanced Displays and Optoelectronics Technologies and Department of Chemical and Biological Engineering, The Hong Kong University of Science and Technology, Kowloon, Hong Kong SAR 999077, China; The Hong Kong University of Science and Technology—Shenzhen Research Institute, Shenzhen 518057, China; orcid.org/0000-0002-5397-0129; Email: eezfan@ust.hk

Authors

Zhu'an Wan — Department of Electronic and Computer Engineering, The Hong Kong University of Science and Technology, Kowloon, Hong Kong SAR 999077, China; State Key Laboratory of Advanced Displays and Optoelectronics Technologies, The Hong Kong University of Science and Technology, Kowloon, Hong Kong SAR 999077, China; The Hong Kong University of Science and Technology—Shenzhen Research Institute, Shenzhen 518057, China

Weiqi Zhang — Department of Electronic and Computer Engineering, The Hong Kong University of Science and Technology, Kowloon, Hong Kong SAR 999077, China; State Key Laboratory of Advanced Displays and Optoelectronics Technologies, The Hong Kong University of Science and Technology, Kowloon, Hong Kong SAR 999077, China; The Hong Kong University of Science and Technology—Shenzhen Research Institute, Shenzhen 518057, China

Suman Ma — Department of Electronic and Computer Engineering, The Hong Kong University of Science and Technology, Kowloon, Hong Kong SAR 999077, China; State Key Laboratory of Advanced Displays and Optoelectronics Technologies, The Hong Kong University of Science and Technology, Kowloon, Hong Kong SAR 999077, China; The Hong Kong University of Science and Technology—Shenzhen Research Institute, Shenzhen 518057, China

Zhilong Song — Department of Electronic and Computer Engineering, The Hong Kong University of Science and Technology, Kowloon, Hong Kong SAR 999077, China; State Key Laboratory of Advanced Displays and Optoelectronics Technologies, The Hong Kong University of Science and Technology, Kowloon, Hong Kong SAR 999077, China; The Hong Kong University of Science and Technology—Shenzhen Research Institute, Shenzhen 518057, China

Chen Wang — Department of Electronic and Computer Engineering, The Hong Kong University of Science and Technology, Kowloon, Hong Kong SAR 999077, China; State Key Laboratory of Advanced Displays and Optoelectronics Technologies, The Hong Kong University of Science and Technology, Kowloon, Hong Kong SAR 999077, China; The Hong Kong University of Science and Technology—Shenzhen Research Institute, Shenzhen 518057, China; orcid.org/0000-0002-5678-5287

Yucheng Ding — Department of Electronic and Computer Engineering, The Hong Kong University of Science and Technology, Kowloon, Hong Kong SAR 999077, China; State Key Laboratory of Advanced Displays and Optoelectronics Technologies, The Hong Kong University of Science and Technology, Kowloon, Hong Kong SAR 999077, China

Chak Lam Jonathan Chan — Department of Electronic and Computer Engineering, The Hong Kong University of Science and Technology, Kowloon, Hong Kong SAR 999077, China; State Key Laboratory of Advanced Displays and Optoelectronics Technologies, The Hong Kong University of Science and Technology, Kowloon, Hong Kong SAR 999077, China; The Hong Kong University of Science and Technology—Shenzhen Research Institute, Shenzhen 518057, China

Feng Xue — Department of Electronic and Computer Engineering, The Hong Kong University of Science and Technology, Kowloon, Hong Kong SAR 999077, China; State Key Laboratory of Advanced Displays and Optoelectronics Technologies, The Hong Kong University of Science and Technology, Kowloon, Hong Kong SAR 999077, China; The Hong Kong University of Science and Technology—Shenzhen Research Institute, Shenzhen 518057, China

Zixi Wan — Department of Electronic and Computer Engineering, The Hong Kong University of Science and Technology, Kowloon, Hong Kong SAR 999077, China; State Key Laboratory of Advanced Displays and Optoelectronics Technologies, The Hong Kong University of Science and Technology, Kowloon, Hong Kong SAR 999077, China; The Hong Kong University of Science and Technology—Shenzhen Research Institute, Shenzhen 518057, China; orcid.org/0000-0002-0493-480X

Wenhao Ye — Department of Electronic and Computer Engineering, The Hong Kong University of Science and Technology, Kowloon, Hong Kong SAR 999077, China; State Key Laboratory of Advanced Displays and Optoelectronics Technologies, The Hong Kong University of Science and Technology, Kowloon, Hong Kong SAR 999077, China; The Hong Kong University of Science and Technology—Shenzhen Research Institute, Shenzhen 518057, China

Complete contact information is available at: https://pubs.acs.org/10.1021/acssensors.5c01908

Author Contributions

Land Wan and W.Z. contributed equally to the work. Z (Zhu'an).W., Z.F., W.Z., and Z.S. conceived and designed the experiments. Z (Zhu'an).W., W.Z., and S.M. performed the material synthesis and device fabrication. C.W. and C.L.J.C. helped with the indoor odor classification demonstration. F.X. and W.Z. contributed to the outdoor hazardous gas monitoring. Z (Zhu'an).W., W.Z., and C.W. contributed to material characterization and analysis. Z (Zixi).W. and W.Y. helped with the gas-sensing performance test and analysis. Y.D. created some diagrams. Z (Zhu'an).W. wrote the manuscript. All authors contributed to the discussion of the results and manuscript revisions.

Notes

ı

The authors declare no competing financial interest.

ACKNOWLEDGMENTS

This work is supported by the National Key Research and Development Program of China (Grant No. 2022YFB3203500), the Hong Kong Innovation Technology Fund (Grant No. GHP/014/19SZ), the Zhongshan Municipal Science and Technology Bureau (Grant No. ZSST21EG05), the Internal Fund of the Hong Kong University of Science and Technology (HKUST; Grant No. IOPCF21EG01), the Center on Smart Sensors and Environmental Technologies, Foshan HKUST Projects (Project Nos. FSUST21-HKUST08D and FSUST21-HKUST09D), and the Foshan Innovative and

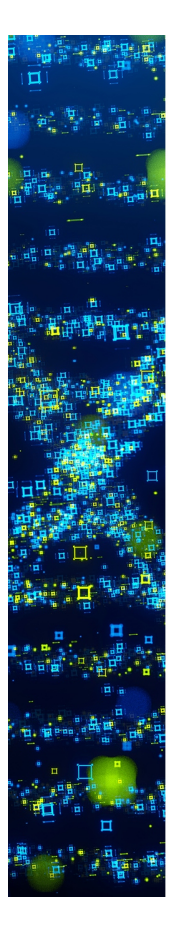
Entrepreneurial Research Team Program (Grant No. 2018IT100031). Special thanks to the Material and Characterization Preparation Facility (MCPF) at HKUST and MNT Micro and Nanotech Co., Ltd. for technical assistance.

REFERENCES

- (1) Zampolli, S.; Elmi, I.; Ahmed, F.; Passini, M.; Cardinali, G. C.; Nicoletti, S.; Dori, L. An Electronic Nose Based on Solid State Sensor Arrays for Low-Cost Indoor Air Quality Monitoring Applications. Sens. Actuators, B 2004, 101 (1), 39–46.
- (2) Wang, C.; Chen, Z.; Chan, C. L. J.; Wan, Z.; Ye, W.; Tang, W.; Ma, Z.; Ren, B.; Zhang, D.; Song, Z.; Ding, Y.; Long, Z.; Poddar, S.; Zhang, W.; Wan, Z.; Xue, F.; Ma, S.; Zhou, Q.; Lu, G.; Liu, K.; Fan, Z. Biomimetic Olfactory Chips Based on Large-Scale Monolithically Integrated Nanotube Sensor Arrays. *Nat. Electron.* **2024**, *7* (2), 157–167.
- (3) Yang, Z.; Liu, Y.; Chen, D.; Miao, J.; Chen, M.; Liu, G.; Gao, G.; Guo, Y.; Cui, D.; Li, Q. A Battery-Free, Wireless, Flexible Bandlike e-Nose Based on MEMS Gas Sensors for Precisely Volatile Organic Compounds Detection. *Nano Energy* **2024**, *127*, No. 109711.
- (4) Yamazoe, N.; Sakai, G.; Shimanoe, K. Oxide Semiconductor Gas Sensors. *Catal. Surv. Asia* **2003**, *7* (1), 63–75.
- (5) Behera, B.; Chandra, S. An Innovative Gas Sensor Incorporating ZnO-CuO Nanoflakes in Planar MEMS Technology. *Sens. Actuators, B* **2016**, 229, 414–424.
- (6) Li, Z.; Yu, J.; Dong, D.; Yao, G.; Wei, G.; He, A.; Wu, H.; Zhu, H.; Huang, Z.; Tang, Z. E-Nose Based on a High-Integrated and Low-Power Metal Oxide Gas Sensor Array. Sens. Actuators, B 2023, 380, No. 133289.
- (7) Zhu, L.; Chen, K.; Zeng, C.; Cao, Q.; Deng, Y.; Yuan, K. In Situ Synthesis of Ordered Macroporous Metal Oxides Monolayer on MEMS Chips: Toward Gas Sensor Arrays for Artificial Olfactory. *Small* **2025**, *21*, No. 2503267.
- (8) Mu, S.; Shen, W.; Lv, D.; Song, W.; Tan, R. Inkjet-Printed MOS-Based MEMS Sensor Array Combined with One-Dimensional Convolutional Neural Network Algorithm for Identifying Indoor Harmful Gases. Sens. Actuators, A 2024, 369, No. 115210.
- (9) Zhang, T.; Tan, R.; Shen, W.; Lv, D.; Yin, J.; Chen, W.; Fu, H.; Song, W. Inkjet-Printed ZnO-Based MEMS Sensor Array Combined with Feature Selection Algorithm for VOCs Gas Analysis. *Sens. Actuators, B* **2023**, 382, No. 133555.
- (10) Kang, K.; Yang, D.; Park, J.; Kim, S.; Cho, I.; Yang, H.-H.; Cho, M.; Mousavi, S.; Choi, K. H.; Park, I. Micropatterning of Metal Oxide Nanofibers by Electrohydrodynamic (EHD) Printing towards Highly Integrated and Multiplexed Gas Sensor Applications. *Sens. Actuators, B* **2017**, 250, 574–583.
- (11) Kwon, H.; Lee, S. H.; Kim, J. K. Three-Dimensional Metal-Oxide Nanohelix Arrays Fabricated by Oblique Angle Deposition: Fabrication, Properties, and Applications. *Nanoscale Res. Lett.* **2015**, 10 (1), 369.
- (12) Hu, Q.-M.; Dong, Z.; Zhang, G.-X.; Li, Y.-X.; Xing, S.-F.; Ma, Z.-H.; Dong, B.-Y.; Lu, B.; Sun, S.-H.; Xu, J.-Q. Ultra-Thin ALD CoOx-ZnO Heterogenous Films as Highly Sensitive and Environmentally Friendly H2S Sensor. *Rare Met.* 2023, 42 (9), 3054–3063.
- (13) Güntner, A. T.; Koren, V.; Chikkadi, K.; Righettoni, M.; Pratsinis, S. E. E-Nose Sensing of Low-Ppb Formaldehyde in Gas Mixtures at High Relative Humidity for Breath Screening of Lung Cancer. *ACS Sens.* **2016**, *1* (5), 528–535.
- (14) Kang, H.; Cho, S.-Y.; Ryu, J.; Choi, J.; Ahn, H.; Joo, H.; Jung, H.-T. Multiarray Nanopattern Electronic Nose (E-Nose) by High-Resolution Top-Down Nanolithography. *Adv. Funct. Mater.* **2020**, *30* (27), No. 2002486.
- (15) Hrachowina, L.; Domènech-Gil, G.; Pardo, A.; Seifner, M. S.; Gràcia, I.; Cané, C.; Romano-Rodríguez, A.; Barth, S. Site-Specific Growth and in Situ Integration of Different Nanowire Material Networks on a Single Chip: Toward a Nanowire-Based Electronic Nose for Gas Detection. ACS Sens. 2018, 3 (3), 727–734.

- (16) Jeong, S.-Y.; Moon, Y. K.; Wang, J.; Lee, J.-H. Exclusive Detection of Volatile Aromatic Hydrocarbons Using Bilayer Oxide Chemiresistors with Catalytic Overlayers. *Nat. Commun.* **2023**, *14* (1), No. 233.
- (17) Kang, M.; Cho, I.; Park, J.; Jeong, J.; Lee, K.; Lee, B.; Del Orbe Henriquez, D.; Yoon, K.; Park, I. High Accuracy Real-Time Multi-Gas Identification by a Batch-Uniform Gas Sensor Array and Deep Learning Algorithm. ACS Sens. 2022, 7 (2), 430–440.
- (18) Lin, Y.; Chen, J.; Tavakoli, M. M.; Gao, Y.; Zhu, Y.; Zhang, D.; Kam, M.; He, Z.; Fan, Z. Printable Fabrication of a Fully Integrated and Self-Powered Sensor System on Plastic Substrates. *Adv. Mater.* **2019**, *31* (5), No. 1804285.
- (19) Ma, S.; Wan, Z.; Wang, C.; Song, Z.; Ding, Y.; Zhang, D.; Chan, C. L. J.; Shu, L.; Huang, L.; Yang, Z.; Wang, F.; Bai, J.; Fan, Z.; Lin, Y. Ultra-Sensitive and Stable Multiplexed Biosensors Array in Fully Printed and Integrated Platforms for Reliable Perspiration Analysis. Adv. Mater. 2024, 36 (24), No. 2311106.
- (20) Jeong, S.-Y.; Kim, J.-S.; Lee, J.-H. Rational Design of Semiconductor-Based Chemiresistors and Their Libraries for Next-Generation Artificial Olfaction. *Adv. Mater.* **2020**, 32 (51), No. 2002075.
- (21) Korotcenkov, G.; Cho, B. K. Metal Oxide Composites in Conductometric Gas Sensors: Achievements and Challenges. *Sens. Actuators, B* **2017**, 244, 182–210.
- (22) Barsan, N.; Koziej, D.; Weimar, U. Metal Oxide-Based Gas Sensor Research: How To? *Sens. Actuators, B* **2007**, *121* (1), 18–35. (23) Liu, M.; Yazdani, N.; Yarema, M.; Jansen, M.; Wood, V.;
- Sargent, E. H. Colloidal Quantum Dot Electronics. *Nat. Electron.* **2021**, *4* (8), 548–558.
- (24) García de Arquer, F. P.; Talapin, D. V.; Klimov, V. I.; Arakawa, Y.; Bayer, M.; Sargent, E. H. Semiconductor Quantum Dots: Technological Progress and Future Challenges. *Science* **2021**, *373* (6555), No. eaaz8541.
- (25) Liu, H.; Li, M.; Voznyy, O.; Hu, L.; Fu, Q.; Zhou, D.; Xia, Z.; Sargent, E. H.; Tang, J. Physically Flexible, Rapid-Response Gas Sensor Based on Colloidal Quantum Dot Solids. *Adv. Mater.* **2014**, *26* (17), 2718–2724.
- (26) Liu, J.; Lv, J.; Shi, J.; Wu, L.; Su, N.; Fu, C.; Zhang, Q. Size Effects of Tin Oxide Quantum Dot Gas Sensors: From Partial Depletion to Volume Depletion. *J. Mater. Res. Technol.* **2020**, 9 (6), 16399–16409.
- (27) Song, Z.; Xu, S.; Liu, J.; Hu, Z.; Gao, N.; Zhang, J.; Yi, F.; Zhang, G.; Jiang, S.; Liu, H. Enhanced Catalytic Activity of SnO2 Quantum Dot Films Employing Atomic Ligand-Exchange Strategy for Fast Response H2S Gas Sensors. *Sens. Actuators, B* **2018**, 271, 147–156.
- (28) Hu, Z.; Zhou, L.; Li, L.; Liu, J.; Li, H.-Y.; Song, B.; Zhang, J.; Tang, J.; Liu, H. Stabilization of PbS Colloidal-Quantum-Dot Gas Sensors Using Atomic-Ligand Engineering. *Sens. Actuators, B* **2023**, 388, No. 133850.
- (29) Xu, X.; Zhuang, J.; Wang, X. SnO2 Quantum Dots and Quantum Wires: Controllable Synthesis, Self-Assembled 2D Architectures, and Gas-Sensing Properties. *J. Am. Chem. Soc.* **2008**, *130* (37), 12527–12535.
- (30) Lin, Q.; Yun, H. J.; Liu, W.; Song, H.-J.; Makarov, N. S.; Isaienko, O.; Nakotte, T.; Chen, G.; Luo, H.; Klimov, V. I.; Pietryga, J. M. Phase-Transfer Ligand Exchange of Lead Chalcogenide Quantum Dots for Direct Deposition of Thick, Highly Conductive Films. *J. Am. Chem. Soc.* **2017**, *139* (19), 6644–6653.
- (31) Sung, Y.; Kim, H. B.; Kim, J. H.; Noh, Y.; Yu, J.; Yang, J.; Kim, T. H.; Oh, J. Facile Ligand Exchange of Ionic Ligand-Capped Amphiphilic Ag2S Nanocrystals for High Conductive Thin Films. ACS Appl. Mater. Interfaces 2024, 16 (3), 3853–3861.
- (32) Kroupa, D. M.; Vörös, M.; Brawand, N. P.; McNichols, B. W.; Miller, E. M.; Gu, J.; Nozik, A. J.; Sellinger, A.; Galli, G.; Beard, M. C. Tuning Colloidal Quantum Dot Band Edge Positions through Solution-Phase Surface Chemistry Modification. *Nat. Commun.* 2017, 8 (1), No. 15257.

- (33) Barsan, N.; Weimar, U. Conduction Model of Metal Oxide Gas Sensors. *J. Electroceram.* **2001**, *7* (3), 143–167.
- (34) Tang, W.; Chen, Z.; Song, Z.; Wang, C.; Wan, Z.; Chan, C. L. J.; Chen, Z.; Ye, W.; Fan, Z. Microheater Integrated Nanotube Array Gas Sensor for Parts-Per-Trillion Level Gas Detection and Single Sensor-Based Gas Discrimination. ACS Nano 2022, 16 (7), 10968–10978
- (35) Kim, H.-J.; Lee, J.-H. Highly Sensitive and Selective Gas Sensors Using P-Type Oxide Semiconductors: Overview. *Sens. Actuators, B* **2014**, *192*, 607–627.
- (36) Lee, J.; Jung, Y.; Sung, S.-H.; Lee, G.; Kim, J.; Seong, J.; Shim, Y.-S.; Jun, S. C.; Jeon, S. High-Performance Gas Sensor Array for Indoor Air Quality Monitoring: The Role of Au Nanoparticles on WO3, SnO2, and NiO-Based Gas Sensors. *J. Mater. Chem. A* **2021**, 9 (2), 1159–1167.



CAS BIOFINDER DISCOVERY PLATFORM™

STOP DIGGING THROUGH DATA —START MAKING DISCOVERIES

CAS BioFinder helps you find the right biological insights in seconds

Start your search

